buildings

MDPI

Article

A Simple Calibrated Ductile Fracture Model and Its Application in Failure Analysis of Steel Connections

Wenchao Li [1] and Yuan Jing [2,*]

[1] School of Civil Engineering, Chang'an University, Xi'an 710061, China
[2] School of Highway, Chang'an University, Xi'an 710064, China
* Correspondence: yjing@chd.edu.cn

Abstract: A new fracture model is developed to predict the ductile fracture of structural steel under multiaxial stress states. First, the Lee–Mear void growth theory is used to establish the quantitative relationship between the stress triaxiality and material's ductility. A stress triaxiality dependence function, which accounts for the material's strain hardening, is derived from modifying the dilatation rate of a spherical void in a typical unit cell. Subsequently, the Tresca failure model is used in conjunction with the Swift hardening law to establish a Lode dependence of fracture strain. Then, the theoretical formula of the new fracture model is obtained by combining both stress triaxiality and Lode angle dependence functions. The proposed fracture model has a unique advantage: i.e., this model has only two material parameters. These two parameters can be easily calibrated through a simple standard coupon test, which significantly reduces the difficulty of model calibration work and facilitates its application in practical engineering. In order to verify the new fracture model, the test results of five types of Q460 steel specimens were used to calibrate the model parameters. The prediction accuracy of the new model is then checked by calculating the average error between the test results and the predicted fracture strain envelope. Finally, the new fracture model was applied in the numerical analysis of two types of steel connections. The validation of the proposed fracture model is verified by comparing the load–displacement curve and failure modes of the steel connections obtained from both test and numerical analysis.

Keywords: ductile fracture model; structural steel; steel connection; fracture prediction

Citation: Li, W.; Jing, Y. A Simple Calibrated Ductile Fracture Model and Its Application in Failure Analysis of Steel Connections. *Buildings* **2022**, *12*, 1358. https://doi.org/10.3390/buildings12091358

Academic Editor: Gianfranco De Matteis

Received: 20 July 2022
Accepted: 26 August 2022
Published: 1 September 2022

1. Introduction

Fracture is one of the major factors inducing the failure of steel structures. It was reported in the Northridge and Kobe earthquakes that severe damage or collapse occurred on many steel frames due to the fracture that occurred at the local regions of the beam-to-column connections [1]. Further, in the 2011 Tohoku-Oki earthquake, fractures were also observed at the connection regions of many braced steel frames, which seriously weakened the bearing capacity of the whole structure [2]. Meanwhile, some experimental research also proves the effect of fracture on the macroscopic behavior of the steel components. Okazaki et al. [3] conducted cyclic loading tests on a series of shear links in eccentrically braced frames and found that the plastic rotation capacity of the link member was controlled by the fracture at the stiffener welds on the web. This phenomenon was also confirmed in the failure analysis of the shear link member conducted by Chao et al. [4]. The above failure events and test results indicate that the fracture behaviors of materials in the vulnerable parts of the steel component control the overall safety of the structure. In this context, investigating the fracture behavior of structural steel and developing an appropriate fracture prediction model becomes a key issue for improving the survivability of steel structures.

The fracture mode of steel structures can generally be divided into two types. The first type of fracture is caused by the geometric defects in the steel components (e.g., the corner,

notches or crack-like defect induced by the manufacturing process). Stress concentrations usually occur at the tip of these geometric defects, which leads to a premature fracture and unstable crack propagation on the steel component. It should be noted that this type of fracture usually results in limited plastic deformation at the fracture region, which is not the research focus of this study. The second type of fracture mainly occurs in the smooth region of the steel component. For this type of failure, a deep plastic deformation combined with an obvious strain localization would occur at the failure region of the member. Microscopic observation analysis shows that this type of ductile fracture is mainly caused by the evolution of micro-void defects inside the material [5,6] and the evolution of these micro-void defects is further affected by the stress state [7–11]. In general, when the material is subjected to a tension-dominated loading, a necking would occur on the investigated material with a local high-stress triaxiality state being formed. Under such a condition, the micro-voids would grow with their volume enlarging, which results in a crack through the coalescence of adjacent voids. On the contrary, when the material is subjected to a shear-dominated loading, a localization shear band with a low-stress triaxiality state would be formed. Then, the micro-voids would evolve with their shape distorting and stretching along the direction of the maximum shear stress with a macro crack being finally formed along the shear localization band. To characterize the effect of stress state on the fracture behavior of the material, two stress state parameters, i.e., stress triaxiality and Lode angle, were proposed in the fracture mechanics' community [12–18], where the stress triaxiality is defined as the ratio of hydrostatic stress to the von Mises equivalent stress, which control the enlargement of micro-void defects, whereas the Lode angle is related to the third invariant of the deviatoric stress tensor, which controls the shape change of the micro-void defects. Both of these two stress parameters can be used to characterize the stress state and control the evolution of the micro-defects during the loading process. In this context, how to accurately determine the quantitative relationship between the stress triaxiality, Lode angle and the evolution of the micro-void defects becomes a key work for developing a reasonable fracture model.

Currently, there are mainly two types of methods, i.e., coupled and uncoupled fracture models that can be used to predict the ductile fracture of metals. The coupled fracture model introduces an internal variable into the constitutive equation of the material to characterize the failure caused by the void defects. The Gurson–Tvergaard–Needleman porous constitutive model [19,20] and continuum damage model [21] are two typical examples of coupled fracture models, where the former uses the void volume fraction as the internal variable to characterize material's plastic damage, whereas the latter defines the evolution of plastic damage according to the thermodynamic potential function. Differently, the uncoupled fracture model defines the constitutive equation and fracture criterion separately. A fracture index, i.e., the fracture strain, is defined as an external warning index in this type of approach to show the limit of the onset of crack at the local material point. Since the uncoupled model has many advantageous features, many uncoupled models were developed in recent decades. Typical examples of uncoupled fracture models include the Xue–Wierzbicki model [22], Bai–Wierzbicki model [23], modified Mohr–Coulomb model [13], Lou–Huh model [15,24], Hosford–Coulomb model [6] and extended unified strength theory [25], etc. Some of these models were successfully applied in the fracture prediction analysis of the steel components. For example, Liao et al. [26] conducted a failure analysis on a typical beam-to-column connection and used the void growth fracture model to predict the fracture initiation and propagation of the crack on the connection. Quan et al. [27] used a modified Mohr–Coulomb fracture model to numerically simulate the ductile failure of the cold-formed steel lap joints. More relevant works concerning the application of fracture prediction methods in the failure analysis of steel components can be found in Refs. [28,29].

It should be noted although the above fracture models provide good approaches for failure analysis of practical structures, a shortcoming remains unsolved for most of these models: i.e., the detailed parameter calibration work of these fracture models is relatively

complex. Generally, to accurately characterize the material's ductility under different stress states, the theoretical formula of most fracture models needs to incorporate a series of material parameters in a phenomenological manner. Correspondingly, calibration of these model parameters requires one to conduct a series of notched specimen experiments and complicated numerical iterations analysis, where such work is apparently not suitable for application in a practical engineering project. In this context, if a fracture model with an easy-calibrated feature could be developed, it will promote the application of the fracture model in practical structural engineering, which is the main objective of this study.

This study aims to develop a simple easy-calibrated uncoupled fracture model to predict the ductile fracture of structural steel under multiaxial stress states. Firstly, the Lear–Mear void growth theory was used to establish the analytical relationship between the stress triaxiality and material's fracture strain, where a simple stress triaxiality dependence function is derived from analyzing the dilatation rate of a spherical cavity in a typical unit cell. Subsequently, the classical Tresca failure criterion is used in conjunction with the Swift hardening law to derive the material's Lode angle dependence function. Then, the theoretical formula of the new fracture model was established by combining both obtained stress triaxiality and Lode angle dependence functions. The proposed new fracture model has two advantageous features: (1) The new model accounts for the influence of the stress triaxiality and Lode angle simultaneously. Thus, this model can be used to predict the failure of structural steel under different stress states. (2) The theoretical formula of the new fracture model contains only two parameters, which can be calibrated via the test data of a standard smooth round bar specimen. This significantly reduces the difficulty of model calibration work. Further, to verify the proposed fracture model, test results obtained from five types of Q460 high-strength steel specimens were used to calibrate the new model. The prediction accuracy of the new model is checked by comparing the experimental data with the prediction results of the model. Finally, the new model is applied to the fracture prediction analysis of two types of steel connections. The validation of the proposed fracture model is verified by comparing the load–displacement curve and failure modes of steel connections obtained from both the test and numerical simulation analysis. The new fracture model proposed in this study provides a quick and convenient tool for engineers to evaluate the ductile failure of steel members.

2. Characterization of Material's Ductility and Stress State

The ductility of a metallic material can be characterized by the accumulated equivalent plastic strain at fracture:

$$\bar{\varepsilon}_f = \int_0^{\bar{\varepsilon}_f} d\bar{\varepsilon}_p \tag{1}$$

where $\bar{\varepsilon}_f$ is the equivalent plastic strain at fracture, and $\bar{\varepsilon}_p$ is the equivalent plastic strain. Generally, the fracture strain of a material is not a constant value. Its magnitude is affected by the stress state.

Stress triaxiality is a stress state parameter for characterizing the degree of hydrostatic pressure. The magnitude of this parameter controls the volume dilatation rate of the micro-void defects inside the material, which, thus, controls the material's ductility. Stress triaxiality is defined as the ratio of mean stress σ_m to the von Mises equivalent stress $\bar{\sigma}$:

$$\eta = \frac{\sigma_m}{\bar{\sigma}} \tag{2}$$

where σ_m denotes the hydrostatic stress, which is equal to the mean value of the sum of the three principal stresses σ_1, σ_2, σ_3, i.e., $\sigma_m = (\sigma_1 + \sigma_2 + \sigma_3)/3$, $\bar{\sigma}$ is the von Mises equivalent stress with its expression represented as:

$$\bar{\sigma} = \sqrt{\left[(\sigma_1 - \sigma_2)^2 + (\sigma_2 - \sigma_3)^2 + (\sigma_3 - \sigma_1)^2\right]/2}$$

Lode angle is a stress state parameter used for characterizing a material's deviatoric stress state. This parameter has a quantitative relationship with the shear stress, which controls the shape of the micro-void defects during the loading process [24]. The value of the Lode angle can be determined through the following functions of J_2 and J_3:

$$\theta = \frac{1}{3}\arccos\left(\frac{3\sqrt{3}J_3}{2J_2^{3/2}}\right) \tag{3}$$

where J_2 and J_3 denote the second and third invariants of the deviatoric stress tensor.

For better understanding, Figure 1 shows a geometrical representation of the Lode angle in the principal stress space, where one can find that the Lode angle θ corresponds to the azimuth angle between the current stress vector OA (used to represent the current stress state) and the projection of the axis of first principal stress σ_1 on the deviatoric stress plane.

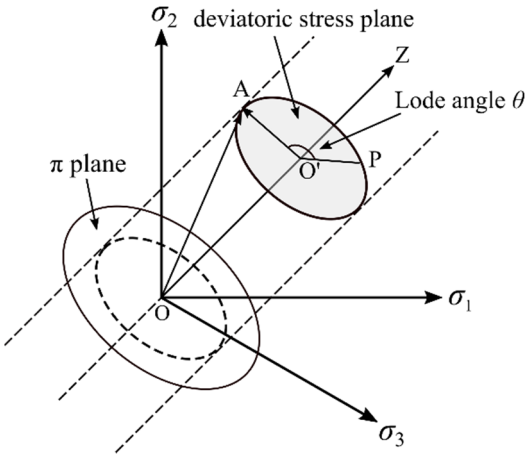

Figure 1. Illustration of the Lode angle in the principal stress space.

It should be noted that the Lode angle θ can be further normalized through the following equation [13,23]:

$$\bar{\theta} = 1 - \frac{6}{\pi}\theta \tag{4}$$

The normalized Lode angle $\bar{\theta}$ in Equation (4) is referred to as the Lode angle parameter [13,23] with its range being $[-1, 1]$. This parameter can be used to characterize the deviatoric stress state of the material, where $\bar{\theta} = 1$ means that the investigated material subjects to a generalized tensile state, $\bar{\theta} = 0$ means that the investigated material subjects to a pure shear or plane strain tensile state, whereas $\bar{\theta} = -1$ means that the investigated material subjects to a generalized compression state. When the magnitude of $\bar{\theta}$ is between the above values, the material undergoes a combined multiaxial stress state.

Since both stress triaxiality and Lode angle parameter affect material ductility, the fracture strain of the investigated material can be expressed as a function of stress triaxiality and Lode angle parameter:

$$\bar{\varepsilon}_f = \bar{\varepsilon}_f(\eta, \bar{\theta}) \tag{5}$$

Equation (5) corresponds to a three-dimensional surface in the space of stress triaxiality, Lode angle parameter and fracture strain. This surface is usually referred to as the fracture envelope, which can be used to characterize material's ductility under different stress states.

Here, if we assume that the dependence of material ductility on the stress triaxiality and Lode angle parameter is independent from each other [30,31], then the fracture strain of the investigated material can be expressed as the following expression:

$$\bar{\varepsilon}_f = \bar{\varepsilon}_{f0}\alpha(\eta)\beta(\bar{\theta}) \tag{6}$$

where $\bar{\varepsilon}_{f0}$ denotes a reference strain value (a material constant), $\alpha(\eta)$ and $\beta(\bar{\theta})$ are referred to as stress triaxiality and Lode dependence functions, which are used to characterize the effect of stress triaxiality and Lode angle on the fracture strain. According to Equation (6), one can find that the key work for establishing a ductile fracture model is to determine the specific form of the two stress state dependence functions, which will be discussed in detail in the following Section 3.

3. Theoretical Derivation of the New Ductile Fracture Model

3.1. Determination of Stress Triaxiality Dependence Function

Since the ductile fracture of metallic materials is induced by the evolution of micro-void defects, the analytical relationship between the stress triaxiality and the material's fracture strain can be obtained from a micro-mechanism analysis on a representative volume element containing a void defect. Lee and Mear [11] conducted an analysis of the growth of a micro-void in a ductile material subjected to a remote tension (see Figure 2). In their analysis, the strain hardening behavior of the investigated material matrix is assumed to obey the following Swift power function:

$$\bar{\sigma} = K\left(\bar{\varepsilon}_0 + \bar{\varepsilon}_p\right)^n \tag{7}$$

where $\bar{\sigma}$ is the equivalent stress, $\bar{\varepsilon}_0$ denotes the initial yield strain, K is a strain hardening parameter, and n is the hardening exponent.

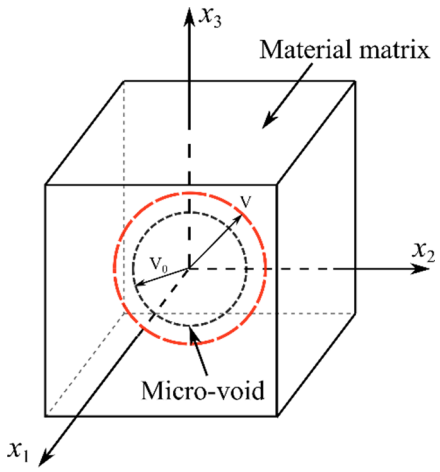

Figure 2. Illustration of a representative element containing a spherical void defect. Remote tensile load is applied along the axis X_3.

Further, assume the micro-void defects inside the material are ideal spherical cavities (see Figure 2), then Lee and Mear derive the following dilatation rate of the spherical cavities by using a numerical method [11]:

$$\frac{dV}{V} = Ed\bar{\varepsilon}_p \tag{8}$$

$$E = \frac{1}{2}\left(\frac{3}{2}n\eta + G\right)^{\frac{1}{n}} \tag{9}$$

$$G = \left(\frac{1}{n} - 1\right)\left(\frac{1}{n} + 0.4319\right)n^2 \tag{10}$$

where $\mathrm{d}V/V$ denotes the dilatation rate of the void defect under remote tension, E is a parameter used to characterize the influences on the void dilatation rate, $d\bar{\varepsilon}_p$ denotes the equivalent plastic strain increment. According to Equations (8)–(10), one can find that the dilatation rate of the spherical void defects is quantitatively controlled by both stress triaxiality η and hardening exponent n.

Further, if we assume that a proportional loading is applied to the investigated material, the stress triaxiality will keep constant. Accordingly, by incorporating Equations (8)–(10) together and integrating on the equivalent plastic strain, we can derive the fracture strain of the investigated material as:

$$\bar{\varepsilon}_f = \frac{C}{[1 + (1.5\eta - 0.5681)n - 0.4319n^2]^{\frac{1}{n}}} \tag{11}$$

where C is a material constant.

Assume that the stress triaxiality and the fracture strain obtained under uniaxial tension are η_0 and $\bar{\varepsilon}_{f0}$, respectively; then, by substituting them into Equation (11), the exact expression of parameter C can be derived as:

$$C = \bar{\varepsilon}_{f0}\left[1 + (1.5\eta_0 - 0.5681)n - 0.4319n^2\right]^{\frac{1}{n}} \tag{12}$$

Then, substitute Equation (12) into Equation (11), a fracture strain formula with an explicit stress triaxiality dependence can be obtained as:

$$\bar{\varepsilon}_f = \bar{\varepsilon}_{f0}\left[\frac{1 + (1.5\eta_0 - 0.5681)n - 0.4319n^2}{1 + (1.5\eta - 0.5681)n - 0.4319n^2}\right]^{\frac{1}{n}} \tag{13}$$

Equation (13) is the fracture strain prediction formula obtained from the classical Lee–Mear void growth theory. This equation was also modified in Ref. [31] to construct an advanced uncoupled fracture model for structural metals. Comparing Equation (13) with Equation (6), one can find that $\bar{\varepsilon}_{f0}$ corresponds to the fracture strain under uniaxial tension and the stress triaxiality dependence function $\alpha(\eta)$ can be obtained as:

$$\alpha(\eta) = \left[\frac{1 + (1.5\eta_0 - 0.5681)n - 0.4319n^2}{1 + (1.5\eta - 0.5681)n - 0.4319n^2}\right]^{\frac{1}{n}} \tag{14}$$

Generally, the value of the stress triaxiality under uniaxial tension is theoretically equal to 1/3 [12], i.e., $\eta_0 = 1/3$. However, since most metals possess an obvious ductility, a necking would always occur on the material under a uniaxial tension before fracture. Accordingly, the stress state at fracture initiation of the material would vary from a uniaxial state to a triaxial state with the value of η_0 increasing, where the exact value of the η_0 depends on the necking degree of the fracture region. Generally, the accurate value of η_0 of the investigated material can be extracted from an associated numerical simulation of the coupon specimen. Since the stress triaxiality at the necking region of the coupon specimen varies during the loading process, the average value of the stress triaxiality is often used for η_0. Some experimental results in the literature show that the average stress triaxiality value under uniaxial tension for the commonly used structural steel is roughly in the range of 1/3–2/3 [32–34]. Table 1 lists the values of η_0 for some typical structural steels. Here, for convenience, we empirically choose an intermediate value 1/2 as the stress triaxiality value under uniaxial tension, i.e., $\eta_0 = 1/2$. Accordingly, the stress triaxiality dependence function becomes:

$$\alpha(\eta) = \left[\frac{1 + 0.1819n - 0.4319n^2}{1 + (1.5\eta - 0.5681)n - 0.4319n^2}\right]^{\frac{1}{n}} \tag{15}$$

Table 1. Values of η_0 for some typical structural steels.

Material	Q345 Steel [32]	Q460 Steel [33]	Q690 Steel [34]
η_0	0.44	0.57	0.64

3.2. Determination of the Lode Angle Dependence Function

Xue [35] proposed a simple Lode angle dependence function for ductile fracture prediction. This Lode angle dependence function is derived by incorporating the Swift

hardening function into the Tresca failure criterion. The specific derivation process for such a function is given as follows.

According to Xue's point of view [35], the maximum shear stress criterion (i.e., Tresca criterion) generally provides a reasonable prediction on the failure stress for most metallic materials. Thus, the fracture stress of the investigated material under different stress state can be expressed as follow:

$$\overline{\sigma}_f = \sigma_{f0} \frac{\sqrt{3}}{2\cos\left(-\frac{\pi}{6}\overline{\theta}\right)} \tag{16}$$

where $\overline{\sigma}_f$ refers to the equivalent stress at fracture, σ_{f0} refers to the fracture stress under uniaxial tension.

In addition, recall that the strain hardening of the investigated material obeys a Swift law in Equation (7); the equivalent stress at fracture $\overline{\sigma}_f$ thus can be expressed as:

$$\overline{\sigma}_f = K\left(\overline{\varepsilon}_0 + \overline{\varepsilon}_f\right)^n \tag{17}$$

Then, according to Equation (17), the fracture stress under uniaxial tension σ_{f0} can be expressed as:

$$\sigma_{f0} = K\left(\overline{\varepsilon}_0 + \overline{\varepsilon}_{f0}\right)^n \tag{18}$$

where $\overline{\varepsilon}_{f0}$ denotes the fracture strain under uniaxial tension ($\overline{\theta}$ = 1). Then, substitute Equations (17) and (18) into Equation (16), the stress-based Tresca fracture model can be converted to the following strain-based form:

$$\overline{\varepsilon}_f = \left(\overline{\varepsilon}_0 + \overline{\varepsilon}_{f0}\right)\left(\frac{\sqrt{3}}{2\cos\left(-\frac{\pi}{6}\overline{\theta}\right)}\right)^{\frac{1}{n}} - \overline{\varepsilon}_0 \tag{19}$$

Generally, the initial yield strain of most metallic materials is relatively small, thus, we can assume $\overline{\varepsilon}_0 \approx 0$. Then, Equation (19) can be simplified as:

$$\overline{\varepsilon}_f = \overline{\varepsilon}_{f0}\left(\frac{\sqrt{3}}{2\cos\left(-\frac{\pi}{6}\overline{\theta}\right)}\right)^{\frac{1}{n}} \tag{20}$$

Equation (20) is the strain-based Tresca failure criterion. Comparing Equation (20) with Equation (6), one can find that, under the assumption of the Tresca failure criterion, the Lode angle dependence function can be derived as:

$$\beta\left(\overline{\theta}\right) = \left(\frac{\sqrt{3}}{2\cos\left(-\frac{\pi}{6}\overline{\theta}\right)}\right)^{\frac{1}{n}} \tag{21}$$

3.3. Theoretical Formula of the New Fracture Model

Since the stress triaxiality and Lode angle dependence functions were established in the previous Sections 3.1 and 3.2, see Equations (15) and (21), then, a new fracture strain prediction formula can be obtained by combining Equations (6), (15) and (21):

$$\overline{\varepsilon}_f = \overline{\varepsilon}_{f0}\left[\frac{1 + 0.1819n - 0.4319n^2}{1 + (1.5\eta - 0.5681)n - 0.4319n^2}\right]^{\frac{1}{n}}\left(\frac{\sqrt{3}}{2\cos\left(-\frac{\pi}{6}\overline{\theta}\right)}\right)^{\frac{1}{n}} \tag{22}$$

Equation (22) is the theoretical formula of the new fracture model. As it can be seen from Equation (22), the new fracture model accounts for the effects of both stress triaxiality and Lode angle on the material's ductility. Thus, this model can be used to predict the failure of structural steel under different stress states. In addition, there are only two parameters, i.e., the hardening index n and the fracture strain under uniaxial tension $\overline{\varepsilon}_{f0}$, which are need for calibration. These two parameters can be easily calibrated via a uniaxial tensile test on a smooth round bar coupon specimen (i.e., the standard test used

for obtaining the engineering stress–strain curve of the investigated material), where the fracture strain under uniaxial tension $\bar{\varepsilon}_{f0}$ can be approximately determined by measuring the geometry of the smooth round bar specimen through the following formula:

$$\bar{\varepsilon}_{f0} = \ln\left(\frac{A_0}{A_f}\right) \tag{23}$$

where A_0 corresponds to the initial cross-sectional area of the smooth round bar specimen, and A_f corresponds to the cross-sectional area at the fracture region (i.e., necking region) of the smooth round bar specimen.

The exact value of the hardening exponent n, which is actually a plasticity material parameter, can be determined by fitting the material's true stress-true strain curve using a reasonable hardening function, e.g., Equation (7). Further, for convenience, this parameter can also be determined through the following equation:

$$n = \frac{\ln\left(\frac{\sigma_{f0}}{\sigma_{y0}}\right)}{\ln\left(1+\frac{\bar{\varepsilon}_{f0}}{\bar{\varepsilon}_0}\right)} \tag{24}$$

where σ_{y0} is the material's initial yield stress, σ_{f0} is the fracture stress under uniaxial tension whose value can be converted from the engineering failure stress through the following equation proposed by Bridgman [36]:

$$\sigma_{f0} = \frac{\sigma_{f,nom}}{\left(1+2\frac{R_f}{r_f}\right)\ln\left(1+2\frac{r_f}{2R_f}\right)} \tag{25}$$

where $\sigma_{f,nom}$ denotes the failure stress obtained from the engineering stress–strain curve of the material, r_f and R_f refer to the minimum cross-section radius and curvature radius of the local fracture region of the smooth specimen. According to the above derivation process, one can find that, compared with other complex ductile fracture models, the fracture model proposed in this study can be easily calibrated through a simple coupon test with the difficulty of model calibration work being significantly reduced. As a result, this new fracture model can be applied easily in the failure analysis of large steel structures.

4. Verification of the New Fracture Model via Structural Steel Notched Specimens

Li et al. [33] conducted fracture tests on five types of specimens (including smooth round bar, notched round bar, pure-shear plate, tensile-shear plate and grooved plate) and obtained the fracture strains of Q460 high-strength structural steel in a wide range of stress triaxiality and Lode angle. Tables 2 and 3 list the mechanical property indexes of the Q460 structural steel and the stress triaxiality, Lode angle parameter and fracture strain from the experiment. It should be noted since the stress triaxiality and Lode angle of each test specimen were variable in the original test, the average value of these two stress state parameters was used to determine the corresponding fracture strain of each specimen (see Table 3). Further, Figure 3 shows the stress triaxiality and Lode angle parameter variation history and the corresponding fracture strain data obtained under the average values of the above two stress state parameters from each test specimen. These experimental data are used to verify the proposed fracture model.

Table 2. Mechanical properties of the Q460 high-strength steel [33].

Young's Modulus E(GPa)	Poisson's Ratio μ	Hardening Parameter K(MPa)	Hardening Exponent n
222.8	0.3	969.14	0.2

Table 3. Experimental data obtained from the Q460 high-strength structural steel specimens [33].

Test No.	Test Specimen	η_{av}	$\bar{\theta}_{av}$	$\bar{\varepsilon}_f$	$\hat{\varepsilon}_{f,\text{new-model}}$	$\hat{\varepsilon}_{f,Tresca}$	$\chi_{i,\text{new-model}}$	$\chi_{i,\text{Tresca}}$	$\Delta_{\text{new-model}}$	Δ_{Tresca}
1	Smooth round bar	0.566	1	1.599	1.452	1.599	0.092	0.000		
2	Notched round bar (Notch radius = 6.25 mm)	0.835	1	0.951	0.999	1.599	0.051	0.681		
3	Notched round bar (Notch radius = 3.125 mm)	1.029	1	0.739	0.776	1.599	0.050	1.165	17.3%	56.8%
4	Notched round bar (Notch radius = 1.5 mm)	1.330	1	0.542	0.536	1.599	0.011	1.951		
5	Pure-shear flat plate	0.106	0.21	1.460	1.487	0.803	0.019	0.450		
6	Tensile-shear flat plate	0.433	0.71	1.264	1.221	1.105	0.034	0.126		
7	Grooved plate (Notch radius = 10 mm)	0.755	0	0.945	0.542	0.779	0.426	0.176		
8	Grooved plate (Notch radius = 3 mm)	0.884	0	0.846	0.456	0.779	0.461	0.080		
9	Grooved plate (Notch radius = 1 mm)	1.204	0	0.524	0.304	0.779	0.420	0.487		

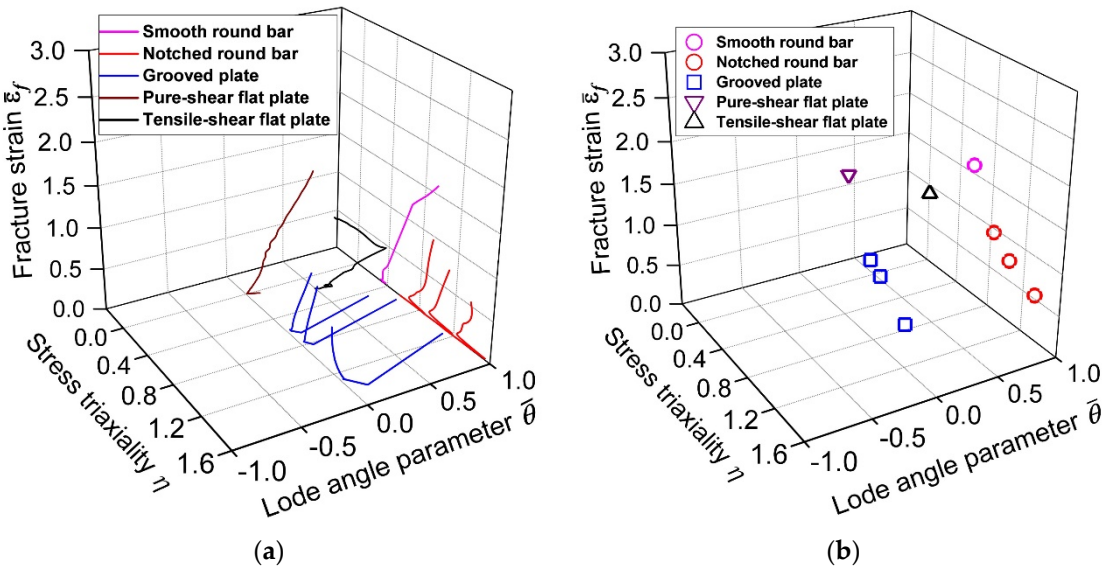

Figure 3. (**a**) Stress triaxiality and Lode angle parameter variation history obtained from each Q460 steel test specimen; (**b**) fracture strain obtained from each Q460 steel test specimen (average values of the stress triaxiality and Lode angle parameter were used to determine the fracture strain) [33].

According to Tables 2 and 3, the hardening exponent n and uniaxial tensile fracture strain $\bar{\varepsilon}_{f0}$ of the Q460 steel can be directly determined through the test result of the smooth round bar specimen, i.e., $n = 0.2$, $\bar{\varepsilon}_{f0} = 1.599$. Then, the fracture strain of the Q460 steel under different stress states can be directly determined through Equation (22). Figure 4a shows the fracture envelope (i.e., the fracture strain surface in terms of the stress triaxiality and Lode angle parameter) of the investigated Q460 steel predicted from the calibrated new fracture model, where the difference between the test data points and fracture envelope is represented by the corresponding vertical error bar. Further, to better distinguish the ductility limit of the material under each stress state, two-dimensional fracture strain locus under generalized tension ($\bar{\theta} = 1$), generalized compression ($\bar{\theta} = -1$), pure-shear and plane strain tension ($\bar{\theta} = 0$) are also shown in the figure. As shown in Figure 4a, the new fracture model can reasonably predict the ductility limit of the Q460 steel under different stress states. The fracture strain data points obtained from each notch specimen (see Table 3) are located close to the fracture strain surface predicted by the new fracture model. Furthermore, to quantitatively investigate the accuracy of the new fracture model, the following formula is used to calculate the prediction error of the new fracture model:

$$\Delta = \frac{1}{N}\sum_{i=1}^{N}|\chi_i| \tag{26}$$

$$\chi_i = \frac{\hat{\varepsilon}_{f,i} - \bar{\varepsilon}_{f,i}}{\bar{\varepsilon}_{f,i}} \tag{27}$$

where Δ denotes the average error between the predicted fracture envelope and the test data, N denotes the number of the tests, χ_i denotes the relative error between the fracture surface predicted by the corresponding fracture model and the ith test data point, $\hat{\varepsilon}_f$ denotes fracture strain predicted from the corresponding fracture model for the ith specimen and $\bar{\varepsilon}_f$ denotes fracture strain obtained from the ith test specimen. By using Equations (26) and (27), the relative and average prediction errors obtained from the new model for the test specimens are calculated and listed in Table 3. The calculation result shows that the average prediction error obtained from the new fracture model for the investigated Q460 steel test specimens is 17.3%. This result satisfies the engineering application accuracy, which verifies the new fracture model.

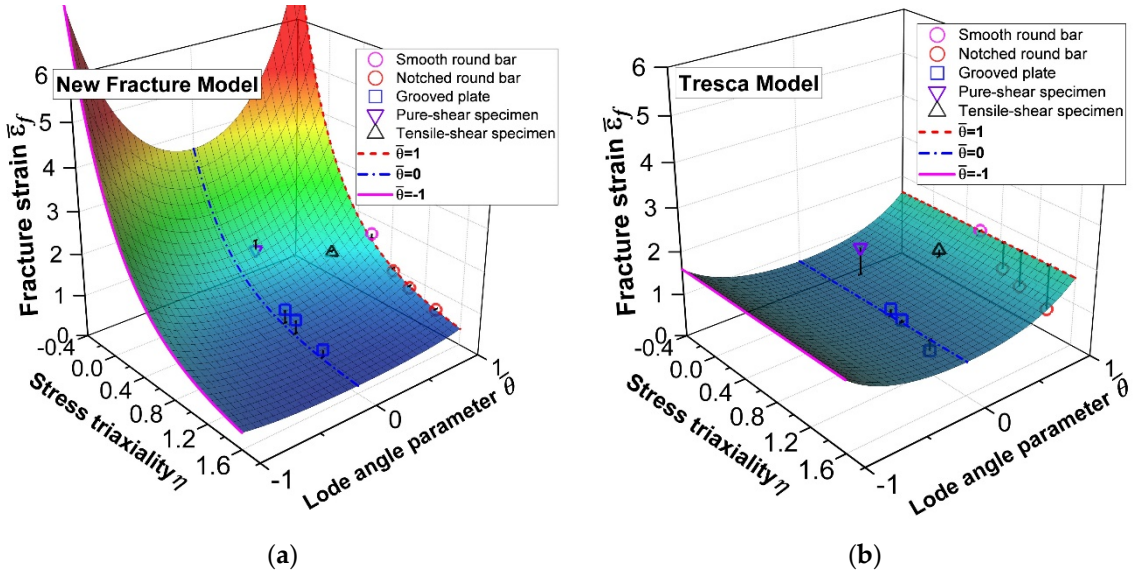

(**a**) (**b**)

Figure 4. Fracture strain envelope of the Q460 structural steel predicted from: (**a**) the new fracture model; (**b**) the Tresca model.

In addition, the Tresca fracture model (Equation (20)) is also calibrated using the test data in Table 3. Since the fracture strain $\bar{\varepsilon}_{f0}$ and the hardening exponent n of the material were determined previously, the fracture strain envelope predicted from the Tresca model can be obtained directly via Equation (20), which is shown in Figure 4b. Further, the relative and average prediction errors obtained from the Tresca model are calculated through Equations (26) and (27), which are listed in Table 3. As can be seen in Figure 4b and Table 3, the prediction results obtained from the Tresca fracture model deviated from the test data significantly with the average prediction error of the model being 56.8%. This error is larger than that obtained from the new fracture model, which also verifies the good prediction accuracy of the new fracture model.

5. Application of New Fracture Model in Failure Analysis of Steel Connections

5.1. Fracture Prediction Analysis of a Welded Beam-To-Column Connection

Chen et al. [37] conducted monotonic tensile tests on a series of welded beam-to-column connections and investigate the mechanical behaviors and failure modes of these specimens. Liao et al. [26] revisit the above experiments and conducted a failure analysis for these test specimens. In this section, the test result of one typical specimen (labeled

as RP-1 specimen) in Refs. [26,37] is used as an example to verify the fracture prediction performance of the new fracture model. Figure 5 shows the geometry and configuration of the RP-1 specimen, which is fabricated by connecting a cold-formed hollow section column (height × width × thickness of the cross-section is equal to 250 mm × 250 mm × 8 mm) with a beam flange plate (width × thickness of the plate is equal to 200 mm × 10 mm) through a penetrated groove weld. Table 4 shows the material used for the RP-1 specimen, where the materials used for the column and flange plate are Q345 steel and that for groove weld is E50 electrode. The detailed material properties for each region on the RP-1 specimen are given in Table 4. It should be noted the column of the RP-1 specimen is formed by a cold bending method. Accordingly, the mechanical properties of the material at the corner region of the column are different from those in other areas (see Table 4). In the experiment, a monotonic tensile loading was applied at one end of the beam flange plate. The loading test stopped until a complete fracture occurred on the connection specimen.

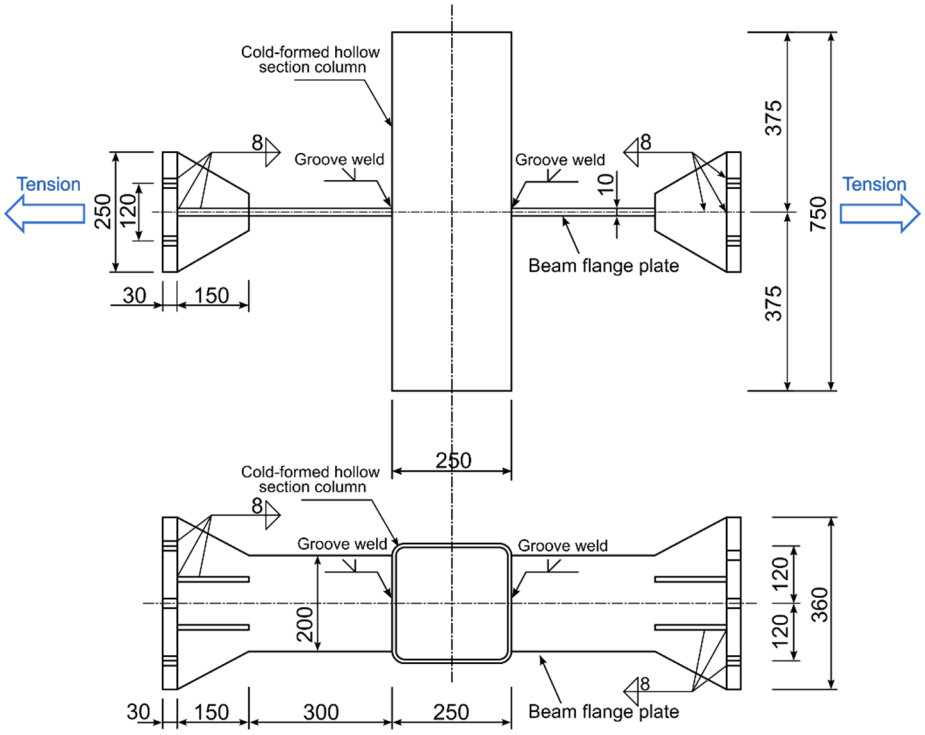

Figure 5. Geometry and configuration of the RP-1 connection specimen (unit: mm) [26,37].

Table 4. Material property at each region RP-1 specimen [26,37].

Specimen Region	Young's Modulus E (MPa)	Yield Strength σ_{y0} (MPa)	Ultimate Strength σ_u (MPa)	Hardening Exponent n	Fracture Strain under Tension $\bar{\varepsilon}_{f0}$
Straight part of the column	2.06×10^5	440.8	533.3	0.085	1.07
Conner region of the column	2.06×10^5	511.0	570.6	0.073	1.03
Beam flange plate	2.06×10^5	380.5	544.1	0.22	1.02
Groove weld	2.06×10^5	380.1	491.3	0.28	1.33

Figure 6 shows the load–displacement curve of the RP-1 specimen obtained from the loading test. It is reported that the fracture was initiated at the exterior junction point between the column flange and groove weld when the displacement at the end of the beam flange reached 6.9 mm (with corresponding tensile force reaching 231 kN simultaneously). Then, the crack propagated along the groove weld and formed a tearing and punching mode fracture surface on the flange of the column.

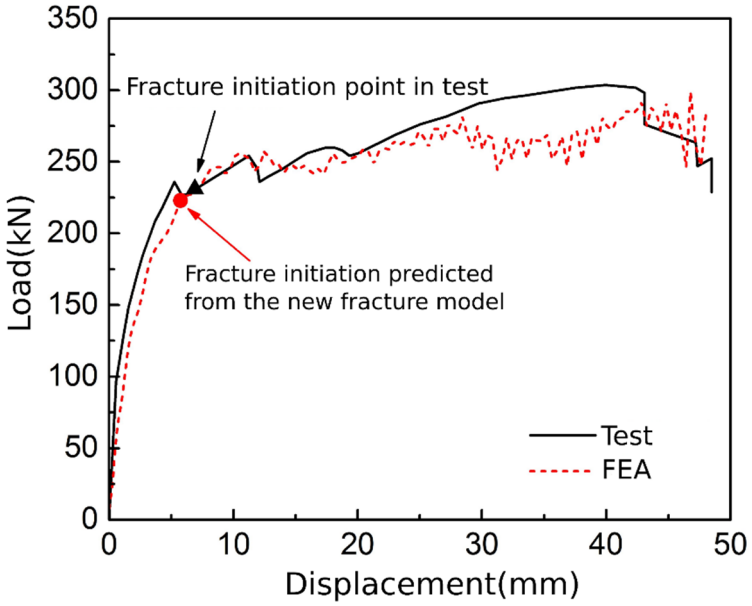

Figure 6. Load–displacement of the RP-1 specimen obtained from the test and finite element analysis.

In order to check the fracture prediction performance of the proposed new fracture model, a parallel numerical simulation is conducted for the RP-1 specimen using the finite element software ABAQUS/Explicit. A general static procedure in the ABAQUS/Explicit is used to conduct the analysis. Figure 7 shows the finite element model of the RP-1 specimen, where the column, beam flange plate and grooved weld are established according to the configurations in Figure 5. In the numerical analysis, a fixed boundary condition is applied at one end of the flange plate. Then, a reference point is created to be coupled with another end of the flange plate to apply the tensile loading to the specimen. In addition, solid reduced integration elements C3D6R are used to mesh the whole model [38]. A corresponding mesh convergence analysis shows that a refined mesh with an element size of 2 mm × 2 mm × 2 mm can be used for the weld region of the specimen to obtain an accurate numerical result. Whereas a relatively coarse mesh is adopted for other regions of the specimen to ensure computation efficiency.

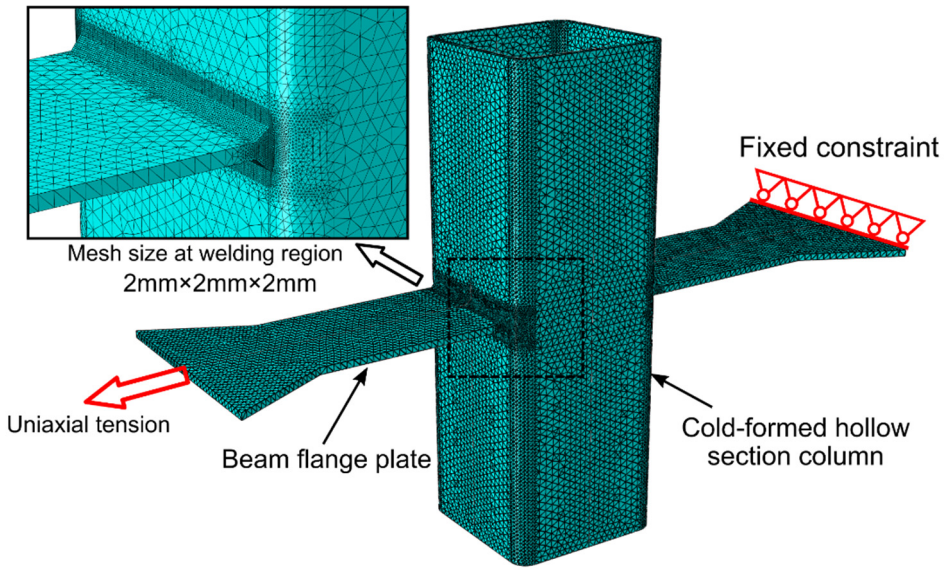

Figure 7. Finite element of the RP-1 specimen.

Furthermore, to ensure a correct response of the connection specimen being obtained from the FE analysis, the von Mises yield criterion combined with an isotropic hardening law is used to describe the mechanical behavior of the materials in each region of the specimen. Figure 8 shows the true stress–plastic strain curve of each material obtained from the corresponding coupon test in the original experiment [26]. Then, the Swift hardening function (Equation (7)) is used to fit and extend these experimental stress–strain curves into a large strain region to simulate the plastic behaviors of the material under large strain conditions (see Figure 8). In the meantime, the values of the corresponding hardening exponent n for each material can also be obtained from the fitting analysis, which is listed in Table 4.

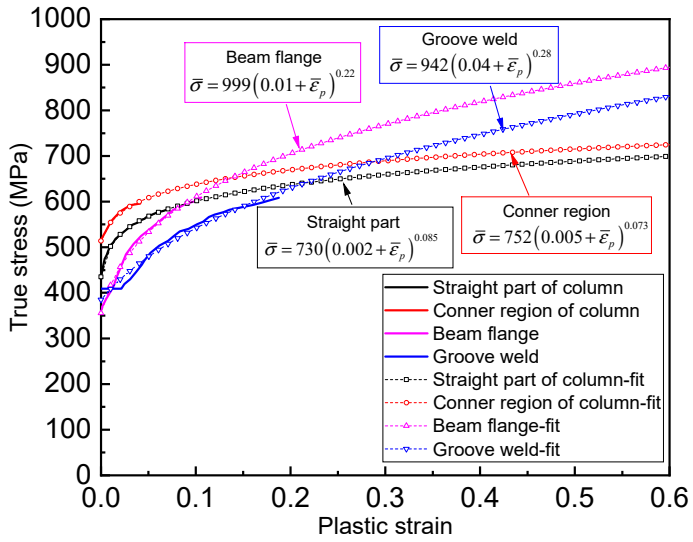

Figure 8. The true stress–plastic strain of each material used for the RP-1 specimen.

In addition, to apply the new fracture model in the numerical analysis of the RP-1 specimen, a built-in "ductile damage" material model provided by the ABAQUS software is used. This material model provides an interface for the user to manually define the values of fracture strain under different stress triaxiality and Lode angle parameters. Then, the fracture is assumed to occur on a material point when the following defined ductile damage index reaches the unity:

$$D = \int \frac{d\bar{\varepsilon}_p}{\bar{\varepsilon}_f(\eta, \bar{\theta})} = 1 \tag{28}$$

In Equation (28), D denotes the ductile damage degree of the material, $\bar{\varepsilon}_p$ and $\bar{\varepsilon}_f$ are the equivalent plastic strain and fracture strain of the material. As it can be seen from Equation (28), when the accumulated equivalent plastic strain reaches the fracture strain limit, the damage index reaches unity with a fracture being initiated.

Since the hardening exponent n and uniaxial tensile fracture strain $\bar{\varepsilon}_{f0}$ for the materials at each region of the specimen have been given in Table 4, the parameters of the new fracture model for each material used for the RP-1 specimen can be directly calibrated. Then, the fracture strain values under different stress triaxiality and Lode angle parameter for each material used for the RP-1 specimen can be determined via Equation (22), which is further input in the "ductile damage" model of each material to predict the initiation of the fracture.

Figure 6 shows the load–displacement curve obtained from the numerical simulation analysis. This load–displacement curve is consistent with the test result, which proves the validation of the numerical simulation analysis. It should be noted there is a minor discrepancy between the numerical and test curves at the elastic loading stage. This discrepancy might be due to the slight difference in the position of displacement extraction

points in the test and numerical simulation analysis. Furthermore, Figure 6 shows the fracture initiation time predicted from the new fracture model, where the corresponding displacement and force at the predicted fracture initiation time are equal to 5.75 mm and 223 kN, respectively. This predicted result is close to the test result (i.e., 6.9 mm and 231 kN) with a prediction error for the displacement and load at fracture being 16.7% and 3.5%, respectively. This result satisfies the accuracy of the engineering application.

Further, Figure 9 shows the crack propagation process and fracture surface of the RP-1 specimen predicted from the new fracture model. The DUCTCRT index in the figure corresponds to the damage index defined in Equation (28). This index is used to characterize the damage degree of the material, where a fracture is assumed to occur when DUCTCRT = 1. As it can be seen from the figure that the fracture was initiated at the exterior junction point between the column flange and groove weld on the specimen. Then, the crack extended along the length direction of the weld and form an obvious tearing and punching fracture surface. This simulated fracture profile is completely consistent with the fracture mode in the original research conducted by Chen et al. [37] (see original Figure 8b in Ref. [37]), which verifies the applicability of the new fracture model in the failure analysis of a practical steel component.

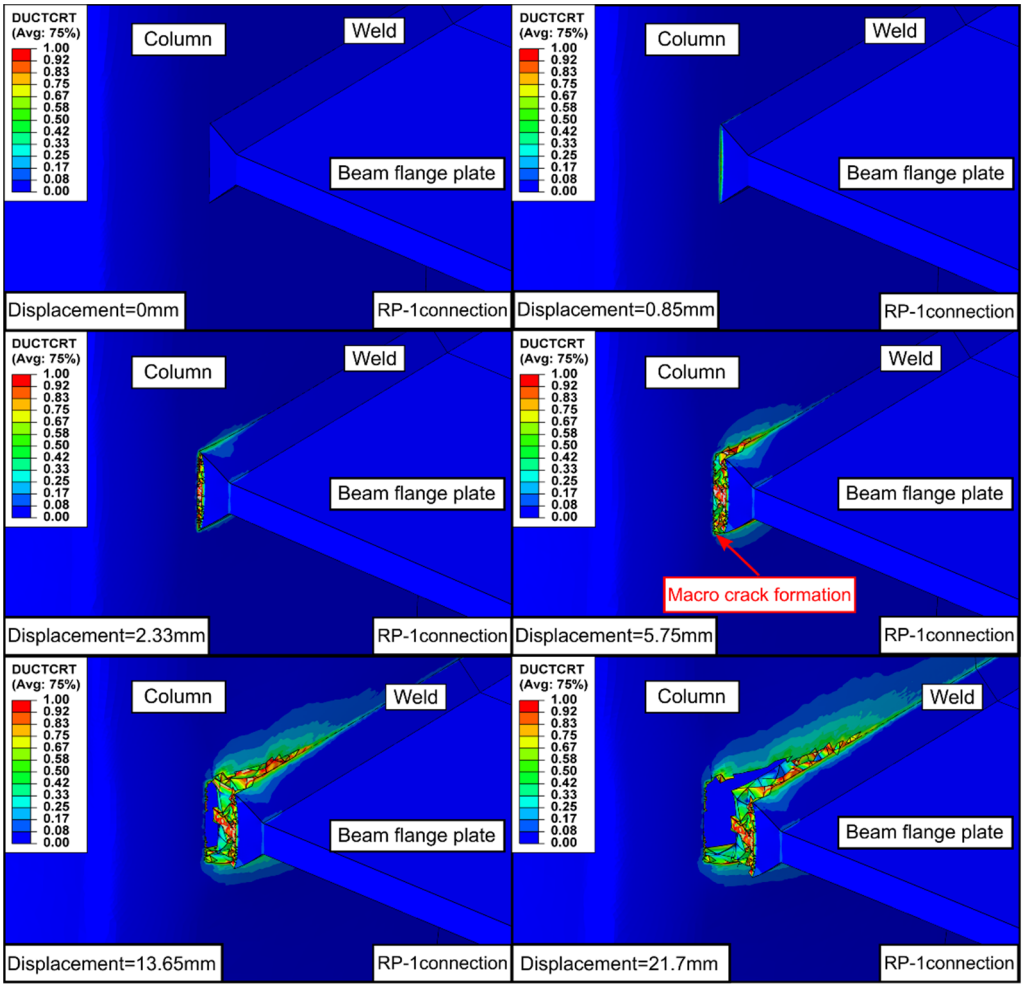

Figure 9. Fracture initiation and crack propagation of the RP-1 specimen simulated from the new fracture model.

5.2. Fracture Prediction Analysis of a CHS Branch to SHS Chord X-Joint

Wang et al. [39] conducted axial tensile loading tests on a group of X-joints, which are made of tubular CHS branches and square SHS chords, and investigate the mechanical behavior of these specimens. Ma et al. [40] revisit the above experiments and conducted

a failure analysis for these test specimens using a ductile damage model. In this section, the test result of the X90-2 joint specimen investigated in the above research is used as an example to verify the fracture prediction performance of the proposed fracture model. Figure 10 shows the geometry and configuration of the X90-2 specimen, where a tubular branch (diameter × thickness of the branch is equal to 180 mm × 10 mm) is connected with a square chord (height × width × thickness of the cross-section is equal to 250 mm × 250 mm × 14 mm) through circumferential fillet welds. The detailed measured leg size of the fillet weld at both upper and lower branches of the specimen is shown in Figure 10. Further, according to Refs. [39,40], the material used for fabricating both chord and branches is Q345B steel, whereas the material used for the fillet weld is E50 electrode. The detailed material properties of the specimen are given in Table 5. In the experiment, an axial tensile loading was applied on the top end plate of the upper branch of the joint. The loading test stops until a complete fracture occurred on the connection specimen.

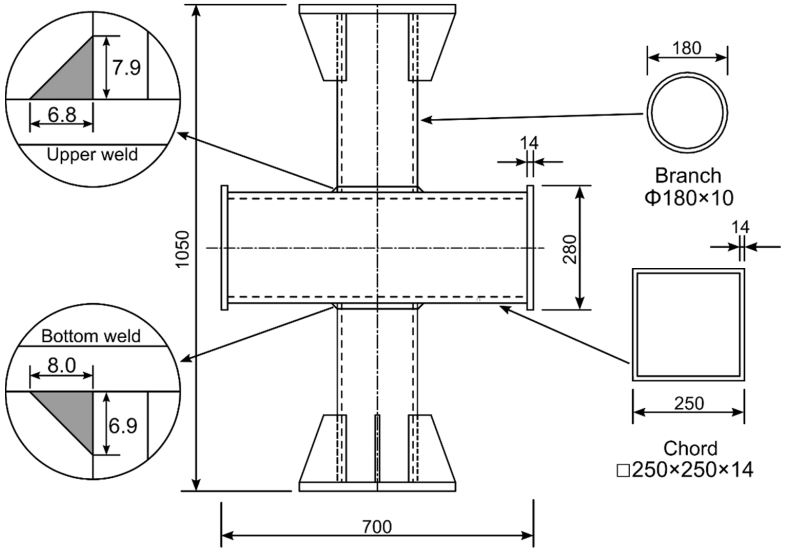

Figure 10. Geometry and configuration of the X90-2 joint specimen (unit: mm) [39,40].

Table 5. Material property at each region of the X90-2 specimen [39,40].

Specimen Region	Young's Modulus E (MPa)	Yield Strength σ_{y0} (MPa)	Ultimate Strength σ_u (MPa)	Hardening Exponent n	Fracture Strain under Tension $\bar{\varepsilon}_{f0}$
Branch	2.06×10^5	375	563	0.16	1.00
Chord	2.06×10^5	325	401	0.187	1.03
Weld	2.06×10^5	416	500	0.156	1.39

Figure 11 shows the load–displacement curve obtained from the top end plate of the X90-2 joint specimen, where the displacement and force at fracture of the specimen correspond to 3.3 mm and 884.8 kN, respectively. During the loading process, the fracture was observed to initiate at the junction point between the chord and fillet weld on the upper branch. Then, the crack propagated rapidly along the weld toe and resulted in a punching shear fracture surface at the wall of the chord [39,40].

Associated numerical simulation analysis of X90-2 joint specimen is carried out using the finite element software ABAQUS/Explicit. Figure 12 shows the finite element model of the X90-2 joint specimen, where the chord, branches, weld and end plate are established according to the geometry and configuration in Figure 10. In the numerical analysis, a fixed boundary condition is applied at the bottom end of the lower branch member. Then, a monotonic tensile displacement is applied at the reference point coupled with the upper end of the branch to simulate the tensile loading of the specimen. In addition,

C3D8R reduced integration solid elements are used to mesh the model. Similar to the methods used in Section 5.1, a refined mesh (with a minimum element size being equal to 1 mm × 1 mm × 3 mm) is adopted at the weld region of the specimen to ensure the fracture initiation and crack propagation are simulated accurately. Meanwhile, a coarse mesh is used for the remaining areas of the specimen to guarantee computation efficiency. It should be noted since the branch and chord are connected by using a circumferential fillet weld, the contact surface between the branch and chord is uncoupled. To correctly reflect this phenomenon, a circumferential seam (gap) is defined at the interface between the branches and chord (see Figure 12). Then, a normal "hard" and tangential frictionless contact property is introduced at these interfaces. Further, the von Mises yield criterion combined with an isotropic hardening law is used to describe the mechanical behavior of the materials at each region of the specimen. Similar to the method used in the previous section, the Swift hardening function is adopted to fit the experimental stress–strain curve of each material on the joint. Then, the fitted stress–strain curves were input into the FE analysis to simulate the plastic behaviors of each material under large strain conditions.

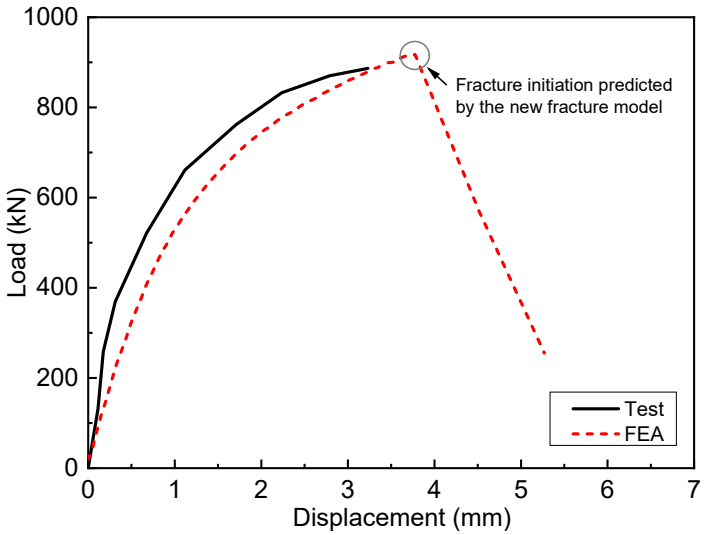

Figure 11. Load–displacement of the X90-2 specimen obtained from the test and finite element analysis.

Finally, since the hardening exponent n and uniaxial tensile fracture strain $\bar{\varepsilon}_{f0}$ of the materials at each region of the specimen were given in Table 5, the parameters of the new fracture model for each material used for the X90-2 specimen can be directly calibrated. Then, the fracture strain values under different stress triaxiality and Lode angle parameters for each material for the X90-2 specimen can be determined via Equation (22), which is further input in the "ductile damage" model of each material to predict the initiation of the fracture.

Figure 11 shows the comparison result on the load–displacement curve of the X90-2 specimen obtained from the test and numerical simulation analysis, where one can find that the load–displacement curve obtained from the numerical simulation analysis is in good agreement with the test. Meanwhile, one can also find that the fracture model proposed in this study can accurately predict the displacement and ultimate strength of the specimen caused by fracture, where the predicted displacement and force at fracture are equal to 3.78 mm and 916.4 kN, respectively. Compared with the test results, this prediction result leads to a prediction error of 15.2% and 3.5% for the displacement and force at fracture, which is in a reasonable range.

Finally, Figure 13 shows the crack propagation process and fracture surface of the X90-2 specimen predicted from the new fracture model. As it can be seen in the figure that the crack initiated at the junction point between the upper fillet weld and the chord wall. Then, the crack extended circumferentially along the root of the fillet weld, which formed

an obvious punching fracture surface on the chord wall. This simulated fracture profile is consistent with the fracture mode shown in the original research conducted in Ref. [40] (see original Figure 13 in Ref. [40]), which verifies the applicability of the new fracture model in the failure analysis of a practical steel component.

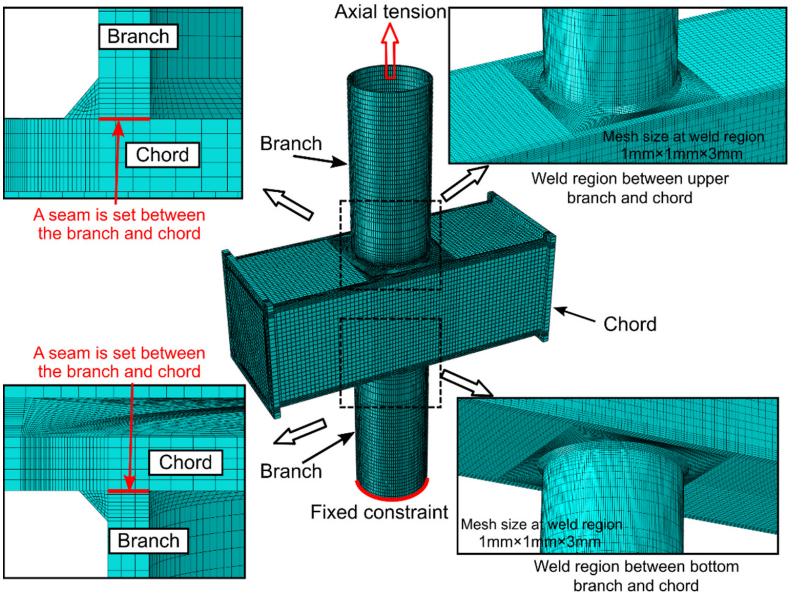

Figure 12. Finite element model of the X90-2 joint specimen.

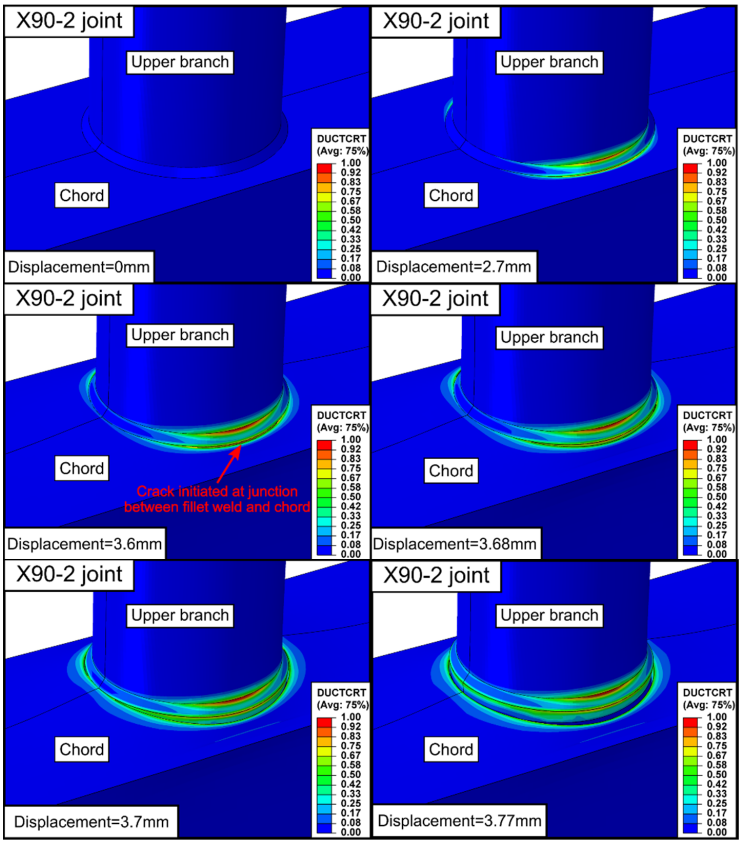

Figure 13. Fracture initiation and crack propagation of the X90-2 specimen simulated from the new fracture model.

6. Discussion

The objective of this study is to propose a simple calibrated fracture model for predicting the fracture initiation of practical steel members. To obtain such a model, the following assumptions were adopted in the theoretical derivation of the new fracture model: (1) The effects of stress triaxiality and Lode angle on the material's ductility are assumed to be independent of each other. Accordingly, the theoretical formula of the stress triaxiality and Lode angle dependence functions can be derived independently from a single specific theory; (2) The influence of the stress triaxiality on the material's fracture strain is derived from the analysis of the dilatation rate of spherical voids in a ductile matrix under axisymmetric loading condition. This stress triaxiality dependence function, obtained under an axisymmetric tension state, is then assumed to be valid for other stress states; (3) The Lode angle dependence of the fracture strain is derived based on the classical Tresca failure criterion. The use of the above assumptions can ensure that an easy-calibrated simplified fracture model can be obtained with the corresponding physical mechanism of materials being properly reflected. However, these assumptions would also bring some limitations, which are discussed below.

6.1. The Correlation between Stress Triaxiality and Lode Angle Dependence

Although the use of the assumption, i.e., the influence of the stress triaxiality and Lode angle parameter on the material's ductility is independent of each other, can simplify the establishment procedure of the theoretical formula of the fracture model, the validity of such a postulation is still controversial. Some studies in the field used such an assumption to establish the theoretical formula of the fracture model [30,31,35] and obtain a good prediction performance in the failure analysis of the practical members [40]. However, some other micro-mechanism analyses on the micro-void defects show that an obvious correlation existed between the stress triaxiality and Lode angle dependences [8]. From the author's point of view, indeed, there is a certain degree of coupling between the stress triaxiality and Lode angle dependence, but how to quantitatively determine this coupling relationship via an analytical method remains a difficult issue. Most current research could only use an indirect method, e.g., changing the classical stress-based failure criterion into a strain-based formula [6,13] or using an empirical formula to fit the numerical result obtained from the representative volume element analysis to obtain such a coupling relationship. However, whether or not the results obtained from these methods are correct is still an open question. In this context, the author believes that the independent assumption on the stress triaxiality and Lode angle for material's ductility is still a good choice for constructing simple engineering used fracture model (rather than a model chasing for absolute accuracy) as long as the prediction results from such a fracture model can fit most test results in a phenomenological manner.

6.2. Validity of Stress Triaxiality Dependence Function for Other Stress States

The stress triaxiality dependence function derived from the Lee–Mear void growth theory is strictly based on the assumption of an axisymmetric tension condition [11]. Correspondingly, whether or not such a triaxiality dependence function is suitable for a more general loading case (i.e., other stress states) needs further verification. Theoretically, the most rigorous method to verify the feasibility of the above axisymmetric model for other loading cases is to conduct a micromechanical analysis on a representative volume element with a spherical void subjected to an arbitrary loading condition. Then, if the evolution function of the micro-void defect obtained from such a unit cell analysis is consistent with that obtained from the axisymmetric model, the feasibility of the axisymmetric model for a general loading case would be verified. However, deriving an elegant analytical solution for the void evolution function under an arbitrary general loading is complicated because most researchers can only use a time-consuming numerical method to establish an empirical relationship for the void evolution. In this context, it would be reasonable to directly extend the stress triaxiality dependence relationship from the axisymmetric model

to other deviatoric stress states as long as the prediction results from the fracture model can fit most experimental results in a phenomenological manner. Such an idea was also used in some research to construct the formula of the fracture models, e.g., Refs. [23,30,35].

6.3. Methods to Improve the Prediction Accuracy of the Proposed Fracture Model

The prediction accuracy of the fracture model is generally related to the number of free parameters in the model. Increasing the amount of the free parameters can enhance the model's flexibility to account for more influence factors on the fracture mechanism of materials, but, on the other hand, would also increase the coupling degree of each influence factor and the difficulty of model calibration. Therefore, how to balance the relationship between the above two points becomes a key work for establishing a fracture model. Since a series of simplified assumptions were used, the fracture model proposed in this study processes only two free material parameters. This feature facilitates the model calibration process but results in limited flexibility for the model to coincide with the test data, which results in relatively low prediction accuracy for the investigated test data in Section 4. In this context, a feasible method to enhance the prediction performance of the fracture model in this study is to further introduce new phenomenological parameters in the theoretical formula of the model, for example, introducing a new parameter before the stress triaxiality term in the stress triaxiality dependence equation (22) to consider other influences (e.g., void shape or material's anisotropy) on material's ductility [31] or use a more advanced failure criterion (e.g., Bai–Wierzbicki failure model [23], which has three free parameters to adjust the failure stress) to derive the Lode angle dependence function. By using such a method, the prediction performance of the proposed fracture model would be enhanced, which is, however, beyond the scope of this study.

7. Conclusions

A new fracture model is proposed to predict the ductile fracture of structural steel under multiaxial stress states. This model is established by combining a stress triaxiality and Lode angle dependence function derived from the Lear–Mear void growth theory and the combination of the Tresca failure criterion and Swift strain hardening law. In order to verify the proposed fracture model, the test results of the Q460 high-strength steel notched specimens and two types of steel connection specimens were used to check the fracture prediction performance of the new model. The main conclusions are summarized as follows:

(1) The proposed new fracture model in this study has a simple theoretical formula with only two material parameters, i.e., the hardening exponent n and fracture strain under uniaxial tension $\bar{\varepsilon}_{f0}$. These two parameters can be easily determined via a uniaxial tensile test on a simple smooth round bar specimen, which significantly reduces the difficulty of model calibration work and facilitates its application in practical engineering.

(2) The proposed new fracture model provides a reasonable prediction on the ductility limit of the Q460 structural steel under different stress states. The three-dimensional fracture envelope determined from the new fracture model is in good agreement with the experimental data of five investigated Q460 steel specimens, with the corresponding prediction accuracy being within 17.3%.

(3) The new fracture model can reasonably predict the fracture initiation and crack propagation of the investigated beam-to-column welded connection and X-joint specimen, which provides a good tool for engineering failure analysis.

(4) The feasibility of the new fracture model needs to be verified by more test data.

Author Contributions: Conceptualization, W.L.; methodology, W.L. and Y.J.; software, W.L.; validation, W.L.; formal analysis, W.L.; writing—original draft preparation, W.L. and Y.J.; writing—review and editing, W.L. and Y.J.; visualization, W.L. All authors have read and agreed to the published version of the manuscript.

Funding: This research was funded by the National Natural Science Foundation of China (Grant No. 51908044 and No. 51908049), the Natural Science Basic Research Plan in Shaanxi Province of China (Grant No. 2020JQ-358) and the Fundamental Research Funds for the Central Universities, CHD (Grant No. 300102282107).

Institutional Review Board Statement: Not applicable.

Informed Consent Statement: Not applicable.

Data Availability Statement: Not applicable.

Conflicts of Interest: The authors declare no conflict of interest.

References

1. Kuwamura, H. Fracture of steel during an earthquake—State-of-the-art in Japan. *Eng. Struct.* **1998**, *20*, 310–322. [CrossRef]
2. Okazaki, T.; Lignos, D.G.; Midorikawa, M.; Ricles, J.; Love, J. Damage to steel buildings observed after the 2011 Tohoku-Oki earthquake. *Earthq. Spectra* **2013**, *29*, 219–243. [CrossRef]
3. Okazaki, T.; Arce, G.; Ryu, H.; Engelhardt, M. Experimental study of local buckling, overstrength, and fracture of links in eccentrically braced frames. *J. Struct. Eng.* **2005**, *131*, 1526–1535. [CrossRef]
4. Chao, S.; Khandelwal, K.; El-Tawil, S. Ductile web fracture initiation in steel shear links. *J. Struct. Eng.* **2006**, *132*, 1192–1200. [CrossRef]
5. Achouri, M.; Germain, G.; Dal, P.; Saidane, D. Experimental characterization and numerical modeling of micromechanical damage under different stress states. *Mater. Des.* **2013**, *50*, 207–222. [CrossRef]
6. Mohr, D.; Marcadet, S. Micromechanically-motivated phenomenological Hosford–Coulomb model for predicting ductile fracture initiation at low stress triaxialities. *Int. J. Solids Struct.* **2015**, *67–68*, 40–55. [CrossRef]
7. Brünig, M.; Gerke, S.; Hagenbrock, V. Micro-mechanical analyses of the effect of stress triaxiality and the Lode parameter on ductile damage and failure. *Int. J. Plast.* **2013**, *50*, 49–65. [CrossRef]
8. Dunand, M.; Mohr, D. Effect of Lode parameter on plastic flow localization after proportional loading at low stress triaxialities. *J. Mech. Phys. Solids* **2014**, *66*, 133–153. [CrossRef]
9. Lou, Y.; Yoon, J.; Huh, H.; Chao, Q.; Song, J. Correlation of the maximum shear stress with micro-mechanisms of ductile fracture for metals with high strength-to-weight ratio. *Int. J. Mech. Sci.* **2018**, *146–147*, 583–601. [CrossRef]
10. Keralavarma, S.; Reddi, D.; Benzerga, A. Ductile failure as a constitutive instability in porous plastic solids. *J. Mech. Phys. Solids* **2020**, *139*, 103917. [CrossRef]
11. Lee, B.; Mear, M. Axisymmetric deformation of power-law solids containing a dilute concentration of aligned spheroidal voids. *J. Mech. Phys. Solids* **1992**, *40*, 1805–1836. [CrossRef]
12. Bao, Y.; Wierzbicki, T. On fracture locus in the equivalent strain and stress triaxiality space. *Int. J. Mech. Sci.* **2004**, *46*, 81–98. [CrossRef]
13. Bai, Y.; Wierzbicki, T. Application of extended Mohr–Coulomb criterion to ductile fracture. *Int. J. Fract.* **2009**, *161*, 1. [CrossRef]
14. Khan, A.; Liu, H. A new approach for ductile fracture prediction on Al 2024-T351 alloy. *Int. J. Plast.* **2012**, *35*, 1–12. [CrossRef]
15. Lou, Y.; Yoon, J.; Huh, H. Modeling of shear ductile fracture considering a changeable cut-off value for stress triaxiality. *Int. J. Plast.* **2014**, *54*, 56–80. [CrossRef]
16. Lou, Y.; Chen, L.; Clausmeyer, T.; Tekkaya, A.; Yoon, J. Modeling of ductile fracture from shear to balanced biaxial tension for sheet metals. *Int. J. Solids Struct.* **2017**, *112*, 169–184. [CrossRef]
17. Roth, C.; Mohr, D. Ductile fracture experiments with locally proportional loading histories. *Int. J. Plast.* **2016**, *79*, 328–354. [CrossRef]
18. Brünig, M.; Gerke, S.; Schmidt, M. Damage and failure at negative stress triaxialities: Experiments, modeling and numerical simulations. *Int. J. Plast.* **2018**, *102*, 70–82. [CrossRef]
19. Gurson, A. Continuum theory of ductile rupture by void nucleation and growth: Part I—yield criteria and flow rules for porous ductile media. *J. Eng. Mater. Technol.* **1977**, *99*, 2–15. [CrossRef]
20. Tvergaard, V.; Needleman, A. Analysis of the cup-cone fracture in a round tensile bar. *Acta Metall.* **1984**, *32*, 157–169. [CrossRef]
21. Lemaitre, J. A continuous damage mechanics model for ductile fracture. *J. Eng. Mater. Technol.* **1985**, *107*, 83–89. [CrossRef]
22. Wierzbicki, T.; Bao, Y.; Lee, Y.; Bai, Y. Calibration and evaluation of seven fracture models. *Int. J. Mech. Sci.* **2005**, *47*, 719–743. [CrossRef]
23. Bai, Y.; Wierzbicki, T. A new model of metal plasticity and fracture with pressure and Lode dependence. *Int. J. Plast.* **2008**, *24*, 1071–1096. [CrossRef]
24. Lou, Y.; Huh, H. Extension of a shear-controlled ductile fracture model considering the stress triaxiality and the Lode parameter. *Int. J. Solids Struct.* **2013**, *50*, 447–455. [CrossRef]
25. Wang, P.; Qu, S. Analysis of ductile fracture by extended unified strength theory. *Int. J. Plast.* **2018**, *104*, 196–213. [CrossRef]
26. Liao, F.; Wang, W.; Chen, Y. Ductile fracture prediction for welded steel connections under monotonic loading based on micromechanical fracture criteria. *Eng. Struct.* **2015**, *94*, 16–28. [CrossRef]

27. Quan, G.; Ye, J.; Li, W. Computational modelling of Cold-formed steel lap joints with screw fasteners. *Structures* **2021**, *33*, 230–245. [CrossRef]
28. Bassindale, C.; Wang, X.; Tyson, W.R.; Xu, S. Analysis of dynamic fracture propagation in steel pipes using a shell-based constant-CTOA fracture model. *Int. J. Pres. Ves. Pip.* **2022**, *198*, 104677. [CrossRef]
29. Jiang, J.; Zhang, H.; Zhang, D.; Ji, B.; Wu, K.; Chen, P.; Sha, S.; Liu, X. Fracture response of mitred X70 pipeline with crack defect in butt weld: Experimental and numerical investigation. *Thin Wall. Struct.* **2022**, *177*, 109420. [CrossRef]
30. Cortese, L.; Nalli, F.; Rossi, M. A nonlinear model for ductile damage accumulation under multiaxial non-proportional loading conditions. *Int. J. Plast.* **2016**, *85*, 77–92. [CrossRef]
31. Li, W.; Jing, Y.; Zhou, T.; Xing, G. A new ductile fracture model for structural metals considering effects of stress state, strain hardening and micro-void shape. *Thin. Wall. Struct.* **2022**, *176*, 109280. [CrossRef]
32. Yan, S.; Zhao, X. A fracture criterion for fracture simulation of ductile metals based on micro-mechanisms. *Theor. Appl. Fract. Mech.* **2018**, *95*, 127–142. [CrossRef]
33. Li, W.; Liao, F.; Zhou, T.; Askes, H. Ductile fracture of Q460 steel: Effects of stress triaxiality and Lode angle. *J. Constr. Steel Res.* **2016**, *123*, 1–17. [CrossRef]
34. Wang, Y.; Li, G.; Wang, Y.; Lyu, Y.; Li, H. Ductile fracture of high strength steel under multi-axial loading. *Eng. Struct.* **2020**, *210*, 110401. [CrossRef]
35. Xue, L. Stress based fracture envelope for damage plastic solids. *Eng. Fract. Mech.* **2009**, *76*, 419–438. [CrossRef]
36. Bridgman, P.W. *Studies in Large Plastic Flow and Fracture*, 2nd ed.; Harvard University Press: Cambridge, MA, USA, 1964.
37. Chen, Y.; Zhang, L.; Wang, T. Experimental study on load carrying capacity of welded joint assemblage between no-diaphragm cold-formed rectangular tube column and flange plate of H-shaped beam under statically tensile load. *J. Build Struct.* **2011**, *32*, 24–31. (In Chinese)
38. D'Angela, D.; Ercolino, M. Fatigue crack growth analysis of welded bridge details. *Frat. Integrità Strutt.* **2022**, *16*, 265–272. [CrossRef]
39. Wang, W.; Gu, Q.; Ma, X.; Wang, J. Axial tensile behavior and strength of welds for CHS branches to SHS chord joints. *J. Constr. Steel Res.* **2015**, *115*, 303–315. [CrossRef]
40. Ma, X.; Wang, W.; Chen, Y.; Qian, X. Simulation of ductile fracture in welded tubular connections using a simplified damage plasticity model considering the effect of stress triaxiality and Lode angle. *J. Constr. Steel Res.* **2015**, *114*, 217–236. [CrossRef]